Generating Initial Conditions for Ensemble Data Assimilation of Large-Eddy Simulations with Latent Diffusion Models

Alex Rybchuk a , Malik Hassanaly a , Nicholas Hamilton a , Paula Doubrawa a , Mitchell J. Fulton b , Luis A. Martínez-Tossas a

^a National Renewable Energy Laboratory, ^b University of Colorado Boulder

ABSTRACT: In order to accurately reconstruct the time history of the atmospheric state, ensemblebased data assimilation algorithms need to be initialized appropriately. At present, there is no standard approach to initializing large-eddy simulation codes for microscale data assimilation. Here, given synthetic observations, we generate ensembles of plausible initial conditions using a latent diffusion model. We modify the original, two-dimensional latent diffusion model code to work on three-dimensional turbulent fields. The algorithm produces realistic and diverse samples that successfully run when inserted into a large-eddy simulation code. The samples have physically plausible turbulent structures on large and moderate spatial scales in the context of our simulations. The generated ensembles show a lower spread in the vicinity of observations while having higher variability further from the observations, matching expected behavior. Ensembles demonstrate near-zero bias relative to ground truth in the vicinity of observations, but rank histogram analysis suggests that ensembles have too little member-to-member variability when compared to an ideal ensemble. Given the success of the latent diffusion model, the generated ensembles will be tested in their ability to recreate a time history of the atmosphere when coupled to an ensemble-based data assimilation algorithm in upcoming work. We find that diffusion models show promise and potential for other applications within the geosciences.

1. Introduction

Given¹ measurements in one part of the atmosphere, can we estimate the unmeasured state of the atmosphere somewhere nearby? On synoptic scales and the mesoscale, the challenge of unmeasured atmospheric flow reconstruction is often addressed through the discipline of "data assimilation" (DA, Carrassi et al. 2018). DA algorithms combine observations with a numerical model of atmospheric dynamics to reconstruct the state of the atmosphere. In recent years, microscale flow reconstruction (~1 m–1 km) has garnered more attention as wind energy researchers seek to better characterize the atmospheric state in the vicinity of a wind turbine (Defforge et al. 2019; Allaerts et al. 2020; Bauweraerts and Meyers 2021; Schepers 2021). While successful microscale reconstructions may rely on the same approaches used at larger scales, microscale flow reconstruction may alternatively necessitate the deployment of new DA algorithms due to increased flow nonlinearity (Carrassi et al. 2018). Other scientific disciplines that study turbulent flows have also recently begun to explore flow reconstruction through traditional DA approaches (Mons et al. 2016; Labahn et al. 2020; Zaki and Wang 2021; Wang et al. 2022) as well as machine learning approaches (Fukami et al. 2019; Stengel et al. 2020; Yousif et al. 2021; Di Leoni et al. 2022; Du et al. 2022; Hassanaly et al. 2022; Yu et al. 2022).

While the field of DA has a wide spread of algorithms, we are particularly interested in ensemble-based approaches here (Evensen et al. 2009; Bannister 2017; Vetra-Carvalho et al. 2018). These approaches reconstruct the state of the atmosphere by simulating the dynamics of multiple plausible atmospheric states, and combining those simulation results with observations. Ensemble-based DA approaches are powerful because the differences between ensemble members can be used to quantify confidence in the reconstructed atmospheric state. This confidence metric is especially important for model validation and uncertainty quantification efforts (National Research Council 2012).

While ensemble algorithms are powerful, they suffer from a major challenge in the context of this paper: if the initial condition of the ensemble members diverges too strongly from the ground truth, ensemble-based DA will often fail. As demonstrated by the classic Lorenz (1963) system, the chaotic dynamics of poorly initialized ensemble members may strongly differ from the dynamics of the ground truth, producing compounding, irreconcilable errors. For mesoscale and synoptic-

¹This Work has been submitted to Artificial Intelligence for the Earth Systems. Copyright in this Work may be transferred without further notice.

scale DA studies, initial estimates for ensemble-based DA can be based off of sources such as reanalysis products. However, microscale atmospheric simulations are conducted using large-eddy simulation (LES) codes (Stoll et al. 2020), and given the recent development of microscale DA, there is no standard approach to initialize atmospheric LES for ensemble-based DA. In purely simulation-based twin experiment studies with a known ground truth and an estimated pair, the estimated initial condition may be generated by adding noise to the hidden ground truth, as is done in, e.g., Evensen et al. (2009, Sec. 9.8 within). However, this approach is not feasible when applied to field campaign measurements. Recent machine learning efforts have shown promise for reconstructing a microscale atmospheric state from sparse measurements (e.g., Diop et al. 2022), though we are unaware of any studies that recreate an ensemble of plausible initial conditions, which is important for ensemble-based DA.

Diffusion models (DMs, Sohl-Dickstein et al. 2015; Song et al. 2021; Luo 2022), and in particular latent diffusion models (LDMs, Rombach et al. 2022), show potential for generating an ensemble of realistic initial conditions for LES. Deep generative models, such as variational autoencoders (Kingma and Welling 2013) and generative adversarial networks (Goodfellow et al. 2014), are a genre of machine learning algorithm that aim to create new samples that follow the same underlying probability distribution function as a training dataset. DMs are a newer category of deep generative model that have achieved state-of-the-art performance on conditional and unconditional 2D image generation tasks (Dhariwal and Nichol 2021), and more recently, they have been applied to 3D conditional state estimation in medical studies (Pinaya et al. 2022). DMs have been shown to generate diverse, high-quality samples but at the cost of slow sample generation (Xiao et al. 2022). Of particular interest to this study, DMs have performed well at the "inpainting" problem (Lugmayr et al. 2022; Suvorov et al. 2022), in which the DM "fills in" a region of a masked image with information that is consistent with the unmasked region. We posit that atmospheric flow reconstruction can be thought of as an inpainting problem, in which observations are taken as the unmasked parts of a sample.

Here, we study the question: given synthetic observations, can we apply an LDM to generate realistic initial conditions for LES? We are specifically motivated to study microscale flow reconstruction by the Rotor Aerodynamics, Aeroelastics, and Wake (RAAW) field campaign (Hamilton et al. 2022), which aims to accurately reconstruct time history of the atmosphere upwind of a

heavily instrumented turbine, so that the measured structural behavior can be compared to predictions from a computational model of the turbine. This paper lays the groundwork for one possible time-history reconstruction approach, in which we could couple initial conditions from an LDM to an atmospheric dynamics code.

We modify the original LDM code (Rombach et al. 2022) to work on three-dimensional samples. We then train an unconditional LDM that generates LES samples that are representative of the training dataset, as well as a conditional LDM that generates plausible LES samples conditioned on synthetic observations (i.e., simulated wind observations that are representative of field measurements). We assess the sample quality using three different approaches: qualitative visualizations, traditional LES metrics (e.g., vertical profiles, turbulence spectra) for realizations from the LDM, and ensemble-based metrics that are used commonly within ensemble forecasting studies. In Section 2, we describe the RAAW field campaign, the configuration of the flow reconstruction problem, and the LES dataset that is used to train and test the LDM. In Section 3, we provide details of the LDM architecture. In Section 4, we study the performance of the LDMs. Finally, in Section 5, we conclude the paper and discuss potential future lines of inquiry.

2. Data: Synthetic Data for the RAAW Field Campaign

The RAAW field campaign (Hamilton et al. 2022) seeks to thoroughly characterize the behavior of a single, utility-scale wind turbine with respect to the incoming flow and the generated wake. While previous field-scale turbine model validation field campaigns (e.g., Doubrawa et al. 2020; Boorsma et al. 2023) have characterized turbine behavior in a time-averaged manner, the RAAW campaign aims to assess time-resolved turbine dynamics on a second-to-second basis over 10-minute periods. To model the turbine dynamics on this timescale, it is critical to accurately reconstruct the time-varying winds flowing into the turbine on the same timescale.

In this study, we conduct a synthetic version of the field campaign, which is sometimes referred to as an "observing system simulation experiment." We simulate a thermally neutral atmospheric boundary layer using the LES code AMR-Wind (Sprague 2021). The domain is forced by U = 10 m s⁻¹ geostrophic winds in the *x*-direction, as well as Coriolis forcing at a latitude of 90°. The LES domain is sized (x, y, z) = (1920, 1920, 960) m with (nx, ny, nz) = (128, 128, 64) grid points, leading to 15-m resolution in all three directions. The simulation uses a fixed 0.5-s timestep. The

LES is initially run for 6 hours to allow turbulence to spin up and become stationary. Afterward, we generate data for the training set by running the LES for 3.5 days and saving the (u, v, w) fields everywhere in the domain every minute, totaling 5,040 samples. After the training set is generated, we generate a test dataset by simulating another 3.5 days after the end of the training dataset period. By using test data from after the training period, we ensure there is no cross-contamination between datasets while also achieving good statistical agreement between the two datasets in our heights of interest, rotor span heights of 56.5-183.5 m (Section 4).

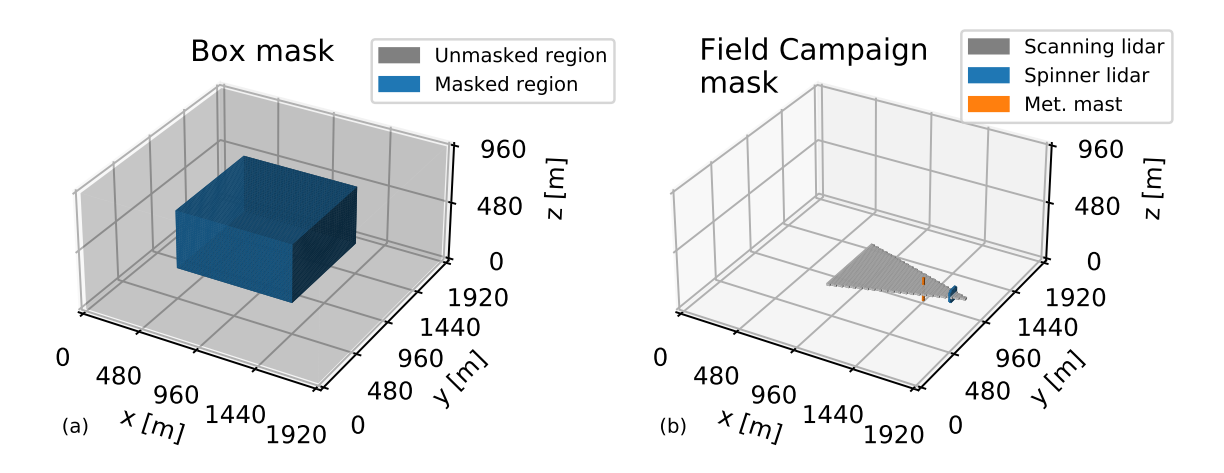


Fig. 1. (a) The masked region and observed region associated with the box mask. (b) The observations associated with the Field Campaign (FC) mask, with each instrument highlighted. The regions without observations are masked.

Synthetic measurements that match the RAAW field campaign deployment are generated by masking regions of the three-dimensional (3D) LES output, and in the context of this paper, we refer to unmasked regions as "observations." We apply the LDM to two sets of masks (Fig. 1). The "box mask" is commonly used in two-dimensional (2D) image inpainting problems (Saharia et al. 2022; Lugmayr et al. 2022), and here, it masks a cube at the center of the domain spanning (64,64,32) grid points. In this configuration, the unmasked data show all three components of velocity. The "Field Campaign (FC) mask" hides data at locations specific to the RAAW field campaign instrumentation layout, displaying data at less than 0.2% of the total volume. This mask could be modified for any other layout of field measurements. All instruments are aligned to point into the incoming wind, as they would be in the field. The turbine can be thought of as sitting at (x,y) = (1800,960) m. The horizontal scanning lidar reaches 1,005 m upwind of the turbine,

covering an azimuthal range of 18° at a height of 120 m. The vertical spinner lidar scan covers the rotor area and sits 120 m upwind of the turbine. The meteorological mast sits 360 m upwind of the turbine and measures in a vertical column between 0 m and 180 m. In this analysis, we make a number of simplifying assumptions regarding measurements in the FC mask.

- We assume that measurements are noise-free.
- We assume that both lidars directly measure the *u*-component of velocity and only this component of velocity. In practice, lidars measure line-of-sight velocity, which is then projected to other directions to obtain specific components of the velocity vector. As our lidars measure directly upstream into the oncoming flow, we believe this assumption is warranted. The meteorological mast measures all three components of velocity.
- We assume that lidars scan instantaneously scan their 2D plane of interest. In practice, both lidars scan across their 2D planes in approximately 2–5 seconds.

3. Methods: Latent Diffusion Models

a. Background

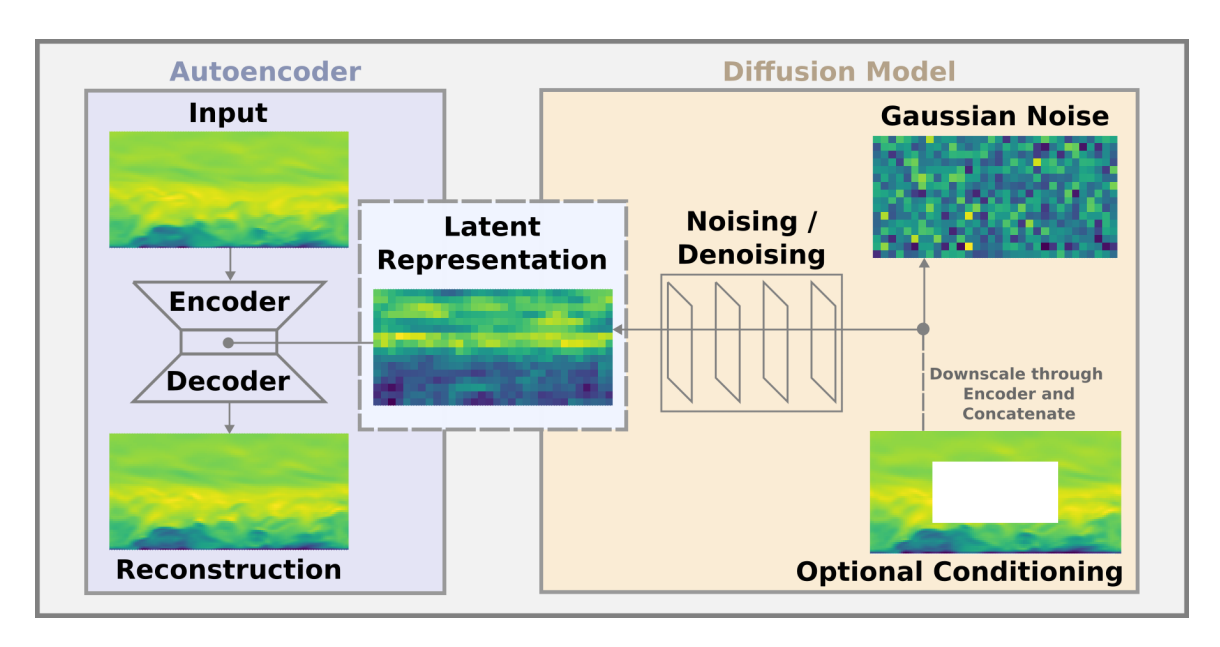


Fig. 2. A schematic depicting the major components of an LDM.

In order to generate synthetic atmospheric states, we employ an LDM (Rombach et al. 2022, Fig. 2), an architecture based on diffusion models (DMs). In recent years, DMs have emerged as

a new category of deep generative model. They were originally developed through the perspective of nonequilibrium statistical physics (Sohl-Dickstein et al. 2015), but they can be derived through the lens of score-based modeling (Song and Ermon 2020) or Markovian hierarchical variational autoencoders (Luo 2022). From one perspective (Song et al. 2021), DMs are trained with the assistance of a prescribed degradation process, in which Gaussian noise is repeatedly added to a sample x over an interval $t \in [0,T]$ until the final sample is indistinguishable from pure Gaussian noise. This process can be thought of as a forward stochastic differential equation

$$dx = f(x,t)dt + g(t)dw$$
 (1)

where f is the drift coefficient, g is the diffusion coefficient, and w is the standard Wiener process. This process can be undone such that the final Gaussian noise state can be reverted to the initial sample using the reverse stochastic differential equation

$$dx = [f(x,t)dt - g(t)^{2}\nabla_{x}\log p_{t}(x)]dt + g(t)d\bar{w}$$
(2)

where \bar{w} is the standard Wiener process for the reverse equation and $\nabla \log p_t(x)$ is the score function, which is challenging to estimate. DMs learn the score function, after which they can be used to draw samples from the probability distribution function $p_0(x)$ (which we will simply refer to as p(x) from here on) that characterizes the training dataset by initially starting with Gaussian noise. Given supplemental information, such as observations or class labels, DMs can draw samples from a conditional probability density function p(x|y) through a number of approaches—for example, training on paired data to directly learn to sample from p(x|y) as is done in Song and Ermon (2020), or by first learning to sample from the unconditional p(x) and then learning an additional conditioning mechanism (e.g., Kawar et al. 2022). We employ the first approach in this study.

While traditional DMs have been shown to generate high-quality images, they can be prohibitively expensive to train for large samples, and three-dimensional samples ares often large. LDMs address this issue by compressing raw, pixel-space samples into a latent space with the use of an autoencoder (AE). The AE is traditionally trained with a mixture of L_1 or L_2 losses, Kullback–Leibler divergence losses as in a variational AE (Kingma and Welling 2013), perceptual losses based on the VGG

network (Zhang et al. 2018), and patch-based adversarial losses (Isola et al. 2018). After the AE is trained, a diffusion model is trained to generate samples in latent space, which can then be converted to pixel space through the AE's decoder.

b. Modifications to the original LDM

We modify the original LDM architecture so that it can be applied to generate synthetic LES data. The exact implementation of the architecture can be found at https://github.com/rybchuk/latent-diffusion-3d-atmopheric-boundary-layer, and we provide a summary of the modifications to the LDM code here.

- The original LDM was developed for 2D images, so we modify the architecture to work on 3D data through the use of operations like 3D convolutions and 3D normalization.
- While the original LDM uses several attention blocks (Brock et al. 2019) throughout the AE, we omit their use there due to the computational demands of a 3D attention block.
- We replace group normalization (Wu and He 2018) with instance normalization (Ulyanov et al. 2017) everywhere except within attention blocks, as we found the latter performed better.
- In the process of selecting the finalized architecture for this paper, we experimented with different weights for each of the loss components in the AE. We also added the option for a physics-based loss that assesses mass conservation by calculating the divergence of the velocity field. In the end, we found the best performance by using an L_1 term, Kullback–Leibler divergence term, and whole-sample adversarial term in the loss function. We omit the VGG-based adversarial loss as well as the mass conservation loss.
- In the original LDM architecture (Rombach et al. 2022), image inpainting is accomplished by first drawing a sample from p(x|y) using unmasked regions as conditioning information. In this scenario, there is no guarantee that the generated sample exactly agrees with the conditioning information y, so inpainting is achieved by overlaying y onto the sample in a postprocessing step. In effect, this treats conditioning information as a hard constraint, meaning the observation is exactly matched in the reconstruction, which makes sense when inpainting images. However, we found this hard constraint would lead to artifacts at the boundaries of FC mask observations, likely because these observations are only one pixel

wide in certain dimensions. As such, we do not postprocess LDM output to exactly match the observations, thereby treating observations as soft constraints, meaning observations are not exactly matched in reconstructions.

c. Network configurations

The LDM requires an AE network for compression to the latent space and decompression. Here, the AE has three input, latent space, and output channels that correspond to the velocity variables (u, v, w). Future work could expand this to learn other quantities like temperature, though we omit temperature here because we study a thermally neutral atmospheric boundary layer. The encoder and decoder of the AE have three internal levels, each with three residual blocks (He et al. 2016), compressing data from (128, 128, 64) to (32, 32, 16). The first internal level uses 16 channels, followed by 32 channels, and then 64 channels. We use a batch size of 2. This network is much smaller than the original LDM used in Rombach et al. (2022, https://github.com/CompVis/latent-diffusion), which, for example, had six internal layers with 128 base channels. Our network is smaller due to computational constraints (we train on two 16-GB VRAM V100s) as well as our large three-dimensional samples.

While our primary goal is to generate candidate velocity fields given FC-style observations, we train both a conditional DM and an unconditional DM to provide more context on network behavior. Both DMs uses the same AE for conversion between pixel space and latent space. The DMs use a UNet architecture (Ronneberger et al. 2015) with three internal layers, respectively using (192, 384, 768) channels, and two residual blocks per layer. Attention blocks are used in the 384 channel layers, 768 channel layers, and the center of the UNet. The DM noise schedule uses 1,000 diffusion steps and is linear. The only difference between the unconditional and conditional DM is the input layer—the unconditional network uses three channels, and the conditional network has an additional four channels, three of which correspond to the compressed observation in latent space and the last of which corresponds to a compressed binary mask corresponding to observed pixels. The conditional DM is exposed to several different masks during training, including box-style and the FC-style observations, in order to increase robustness and potentially accuracy (Saharia et al. 2022). The same conditional DM is then used to produce both box-style and FC-style samples.

4. Results

a. Qualitative performance

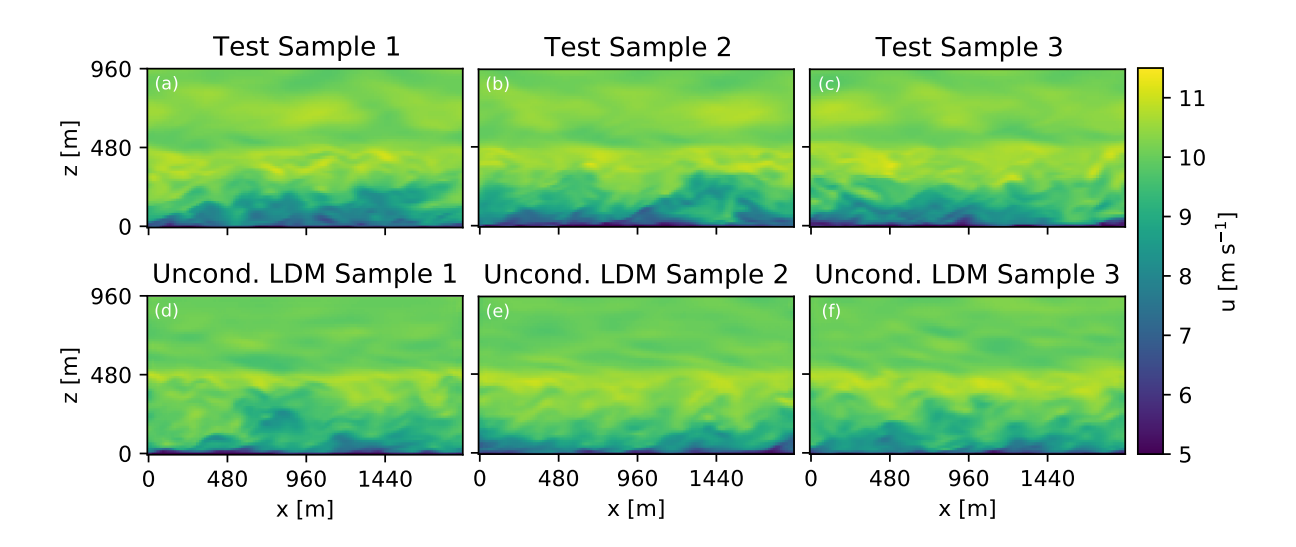


Fig. 3. (a)–(c) Streamwise cross sections of u at y = 960 m from ground truth, test data. (d)–(f) Same as above, except for samples from an unconditional LDM.

Before quantitatively assessing the LDM, we first qualitatively compare multiple samples from an unconditional LDM to ground truth testing data by looking at cross sections of u (Fig. 3). We include cross sections of v and w as well as three-dimensional isocontours in Appendix A. At a high level, all LDM samples qualitatively look like a turbulent atmospheric boundary layer. The generated samples have winds that are generally slow near the ground and stronger aloft until they hit the capping inversion near 480 m, above which the winds are less turbulent. The LDM turbulent structures look like turbulent structures in the ground truth data. The horizontal boundaries of the samples are periodic, just as they are in the testing data. Crucially, however, closer inspection reveals that the LDM samples appear slightly smoother than the ground truth data. This discrepancy on smaller scales is further characterized in Section 4b.

The samples generated using the conditional LDM and the box mask look similarly good, while also accommodating information from unmasked regions (Fig. 4). We visualize a u cross section of a ground truth sample, the associated box mask observation, one conditionally generated sample, and the mean and standard deviation from n = 100 conditionally generated samples. We include additional visualizations for other samples in Appendix B. The conditional samples look similar to

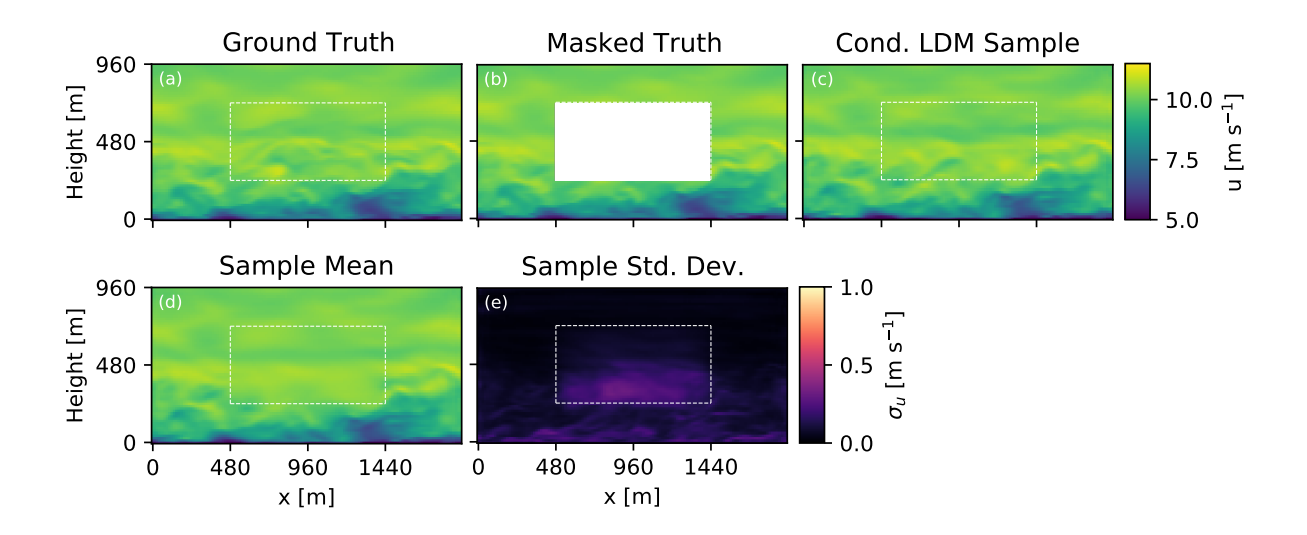


Fig. 4. Streamwise cross sections of u at y = 960 m for (a) a ground truth sample, (b) the box observation created from the ground truth sample, and (c) one sample from the conditional LDM, given the observation. (d) The mean from n = 100 conditional LDM samples. (e) The standard deviation from n = 100 conditional LDM samples. All subpanels display a white dashed line as a reference to the mask.

the unconditional samples, except the perimeter of the conditional sample and the averaged field is relatively unchanged. The transition between the unmasked and the masked region is smooth and does not display any artifacts. This smooth transition is in part achieved by treating observations as a soft constraint instead of a traditional inpainting hard constraint, in which the exact values of the observations would be superimposed over the unmasked region. The statistical behavior of the conditional predictions qualitatively matches expected behavior. Beneath the capping inversion, the mean prediction is smooth, which is expected in a turbulent region. The mean prediction also clearly displays the capping inversion, above which the mean flow structures inside the masked region agree well with the structures in the unmasked region. Inside the unmasked region, the standard deviation of LDM predictions is largest at the bottom of the mask and smaller aloft. This aligns with physical behavior and is expected, as mean shear gradients at the surface encourage mechanical generation of turbulent kinetic energy and therefore wind speed variance. The LDM also displays nonzero standard deviation in the unmasked regions, which would not be the case if we treated observations as a hard constraint.

Finally, the conditional samples for the FC mask (Fig. 5) also match the quality of the previously discussed samples, even though they are conditioned on minimal data. For the particular

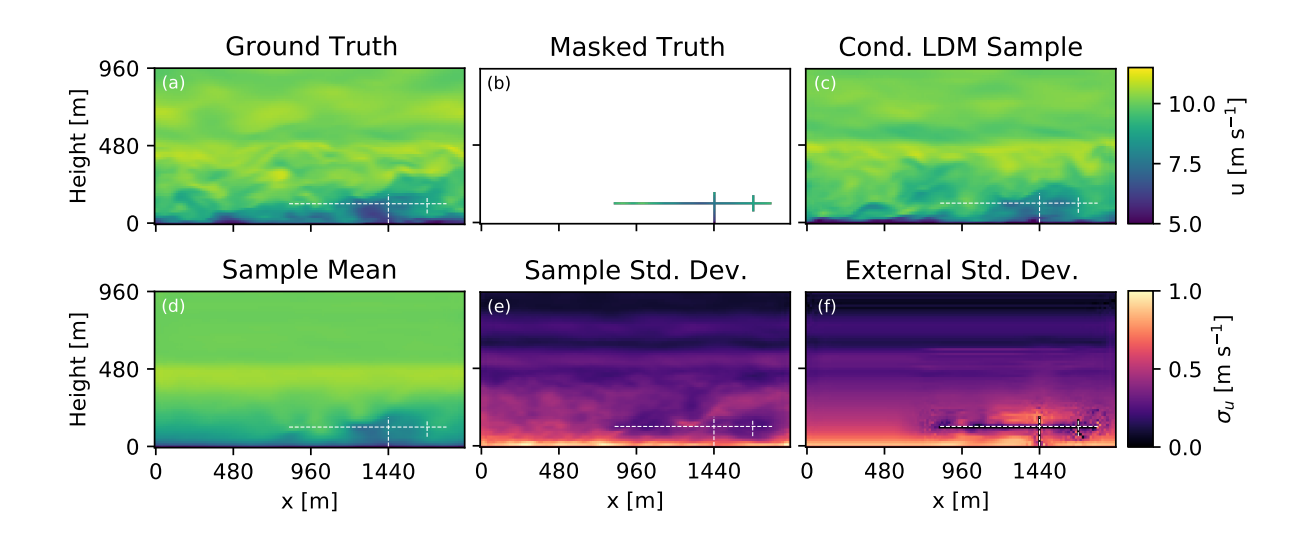


Fig. 5. (a)–(e) Same as Fig. 4, except for the FC mask. (f) As discussed in Section 4c, an external estimate of the conditional standard deviation for the observation in panel (b).

observation shown in Fig. 5, there is a region of slow *u*-wind in the vicinity of the measurements. Correspondingly, each of the samples also has a patch of slow wind in the same area. This flow structure is especially clear in the mean prediction (Fig. 5d), and qualitatively, the mean prediction aligns well with the ground truth in the vicinity of the observations. Away from the observations, the mean prediction becomes much smoother, showing that the conditioning only has local effects, as would be expected in a turbulent flow. The standard deviation of the predictions for the FC mask (Fig. 5e) also show a smaller standard deviation in the vicinity of the observations, especially near the horizontal lidar measurement. Thus, the conditioning is reducing the sample-to-sample spread near the measurements, as desired. The FC samples exhibit much higher variance than the box mask samples (Fig. 4e), as would be expected because the FC samples are conditioned on a smaller region.

After assessing the visual quality of samples, we return to the primary research question raised in the introduction and qualitatively demonstrate that LDM samples act as compatible initial conditions for our LES code. We generate a FC mask sample using the observation in Fig. 5 and then use it as the initial condition in a 1-hour LES simulation. We create a video that visualizes a time history of a streamwise cross section and a top-down view of the simulation at https://github.com/rybchuk/latent-diffusion-3d-atmopheric-boundary-layer. The simulation successfully runs and does not display any obvious numerical artifacts such as discontinuities in the

flow field around the masked region or ringing in the form of waves or instabilities. Thus, this video demonstrates that LDM samples can successfully serve as initial conditions, and as such, they show promise for initializing an ensemble-based DA method.

b. Physical assessment of LDM samples

We next quantitatively assess the performance of the LDMs against physical aspects of the LES: vertical profiles of velocity components and kinematic fluxes, probability density functions of velocity components, turbulence spectra, and mass conservation. For completeness, we compare LDM statistics to those from both the training dataset and testing dataset. These two datasets have different statistics, as they come from distinct simulation periods. However, their statistics match within our region of interest (rotor disk heights), thereby improving the probability of success for our flow reconstruction problem.

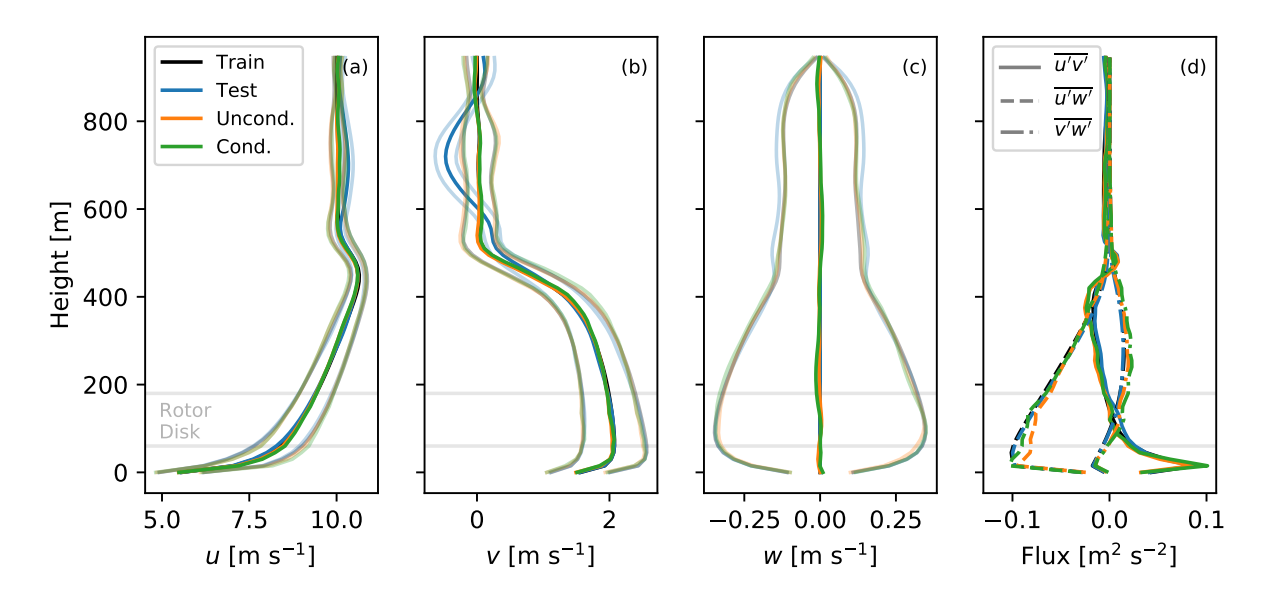


Fig. 6. (a)–(c) Vertical profiles of horizontally averaged velocity components from training data, testing data, unconditional LDM samples, and FC-mask conditional LDM samples. Averages are shown as solid lines, and ±1 standard deviations are shown as faded lines. (d) Kinematic fluxes of the same data.

The LDM accurately captures average velocity profiles (Fig. 6a–c), while slightly underperforming on kinematic velocity profiles (Fig. 6d). We compare horizontally averaged profiles from the training dataset, testing dataset, n = 100 unconditional samples, and n = 100 conditional samples from the FC mask. The mean and standard deviation of LDM velocity profiles agree well

with training data at all heights, and with testing data beneath the capping inversion. Thus, the LDM performs well on first-order statistics. However, the LDMs do show some deviations when comparing kinematic fluxes, a second-order statistic that is more challenging to capture than the mean. In particular, the unconditional LDM underestimates the downward flux $\overline{u'w'}$ by as much as 20% between 15 m and 150 m. The conditional LDM performs better in this region with only an 8% discrepancy, possibly because of the near-surface conditioning information.

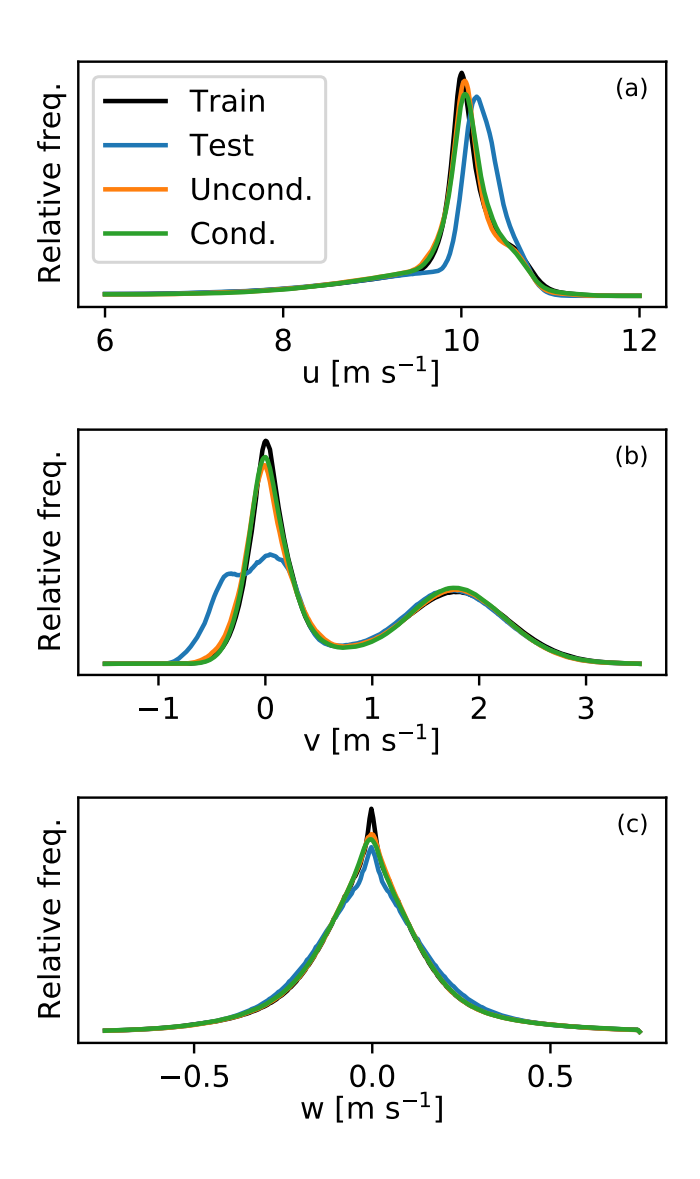


Fig. 7. The probability distribution function for training data, testing data, unconditional LDM samples, and conditional LDM samples for (a) u, (b) v, and (c) w.

Similarly, the probability distribution functions (pdfs) of velocity components show broad agreement, while missing fine-scale details (Fig. 7). We calculate velocity distributions using the same three-dimensional data that was used to calculate average vertical profiles. The pdfs from LDM samples match the pdfs from training data well at all locations except for the peaks. We note that the pdfs of u and v from testing data show a large discrepancy from those from the training data here. This discrepancy comes from velocity differences above the capping inversion, and as such, does not impact performance in our region of interest.

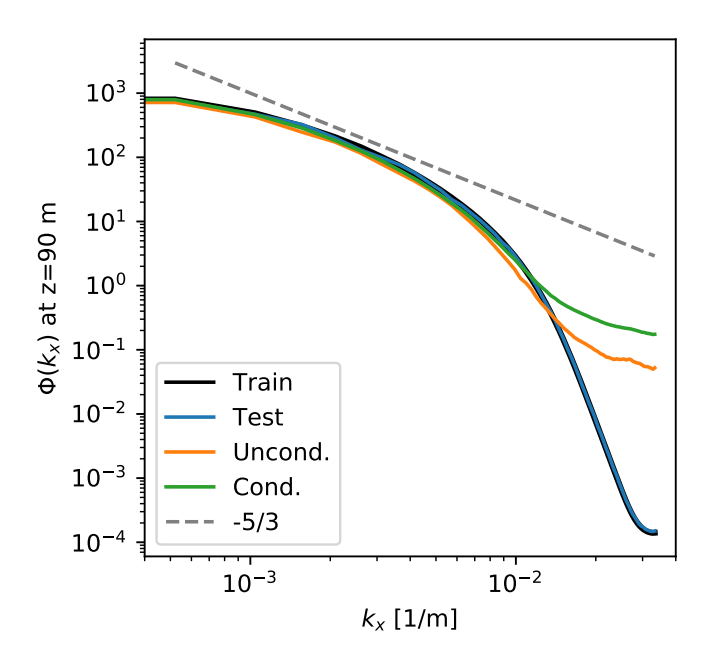


Fig. 8. The turbulence spectra of u at z = 90 m for training data, testing data, unconditional LDM samples, and conditional LDM samples.

While the power spectra of LDM samples match ground truth at large spatial scales, the LDM spectra have too much energy at the smallest spatial scales (Fig. 8). We calculate one-dimensional spectra of u at a height of 90 m. The LDM and ground truth spectra have similar values for wavenumbers smaller than 0.01 m⁻¹, and the LDM accurately captures the inertial scale of turbulence, as visualized by the -5/3 slope. However, for wavenumbers larger than 0.01 m⁻¹, the LDM has too much energy. It makes sense that the large scales are well represented, as the autoencoder part of the network seeks to minimize the L_1 of the samples, thereby prioritizing reconstructing fields on the largest spatial scales. As such, the smallest scales have a relatively small impact on the loss function.

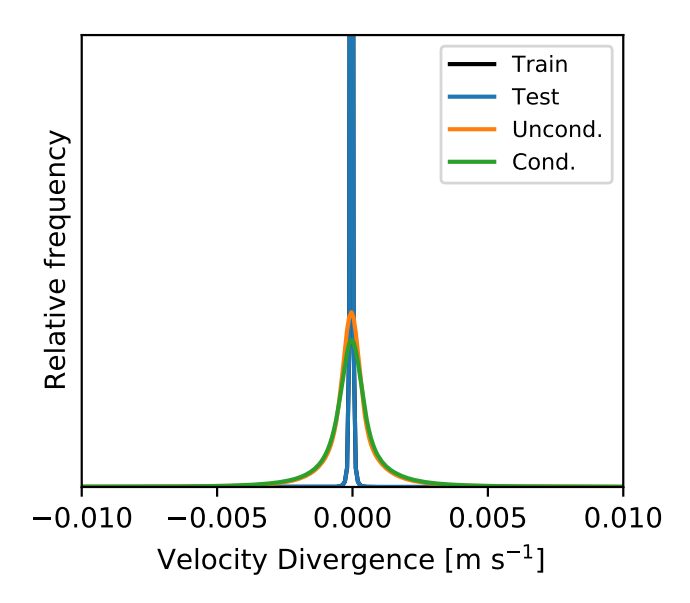


Fig. 9. An assessment of mass conservation, as visualized by distributions of velocity divergence for training data, testing data, unconditional LDM samples, and conditional LDM samples. Training and testing distributions sit on top of one another.

Finally, we assess the LDM's ability to satisfy mass conservation by examining distributions of velocity divergence $\frac{\partial u_i}{\partial x_i}$ (Fig. 9). If continuity were exactly satisfied, the distribution of divergence would be shaped like a Dirichlet function at $\frac{\partial u_i}{\partial x_i} = 0$. The testing and training data approximately satisfy this behavior, showing small deviations from 0 due to numerical artifacts. While distributions for both the unconditional and conditional LDM data show a spike centered on 0, their spikes are not nearly as sharp. Thus, the LDMs appear to have some awareness of mass conservation, but they do not satisfy it here as well as the ground truth data.

c. Ensemble-oriented assessment

1) Rank histogram analysis

For ensemble-based flow reconstruction, it is important to have a well-calibrated ensemble (Wilks 2019, Section 9.7). Ensemble members are drawn from some pdf, and in an ideal scenario, the ground truth would be seen as just another draw from that pdf, such that the ground truth is statistically indistinguishable from the ensemble members, a condition termed "ensemble consistency."

Ideally, the simulated ensemble would show zero bias relative to the ground truth, and the ensemble should have an appropriate but not excessive amount of spread.

One common approach to assess ensemble consistency is the rank histogram (Hamill 2001). When given a group of predictions, the rank of the ground truth is calculated by sorting the ensemble members from smallest to largest by some scalar quantity (e.g., *u* at a particular grid cell), and then identifying the position of the ground truth relative to the ensemble members. When repeated for several reconstructions, rank calculations can be collected into a rank histogram, a diagram that can diagnose ensemble bias as well as overconfidence or underconfidence.

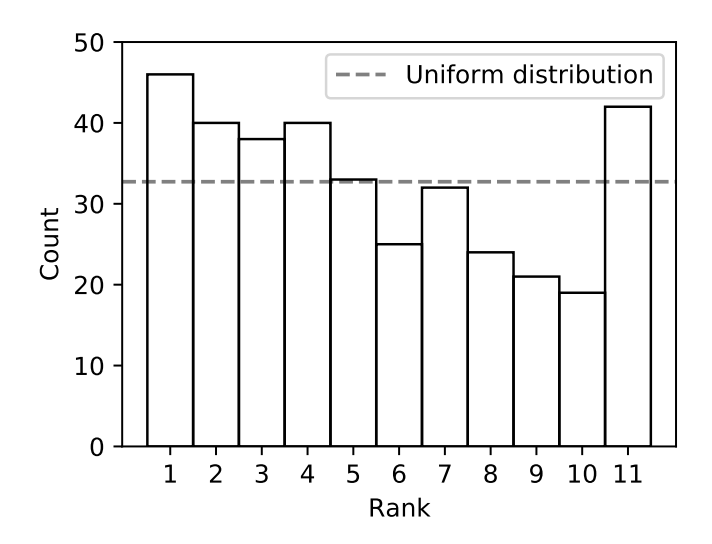


Fig. 10. Rank histogram for u at the turbine nacelle, given 10-member LDM FC ensembles for 360 observations.

We assess ensemble quality by compiling a rank histogram using the first 6 hours (360 observations) from the test set and generating 10 ensemble members per observation (Fig. 10). We calculate the rank of each ground truth by examining u at the unobserved grid cell immediately downwind of the first scanning lidar observation, a cell that can be thought of as the turbine nacelle. An ideal rank histogram would look like a uniform distribution. However, the rank histogram here looks like a combination of a U-shape and a downward linear slope. The U-shape shows that LDM samples are underly diverse—the ground truth disproportionately falls at one extreme of the ensemble. The downward slope indicates that the ground truth tends to be disproportionately smaller than the rest of the ensemble, or in other words, the ensemble often overpredicts. We verify this by calculating the bias of the LDM samples relative to their respective ground truths,

finding that u is on average 0.02 m s⁻¹ higher. Thus, while the downward slope suggests a tendency to overpredict u at turbine hub height, the near-zero bias is balanced out by the right arm of the U-shaped distribution. In the end, the LDM ensembles deviate from ideal behavior, which is in practice the case even for skillful ensemble forecasts (e.g., Monache et al. 2013; Ravuri et al. 2021). These deviations may be small in the end, and future work will use these ensembles in a data assimilation process and assess if the unoptimal behavior is problematic in practice.

2) External estimate of conditional standard deviation

While rank histograms assess ensemble consistency and are used primarily in the ensemble weather forecasting field, we can alternatively assess the ensemble quality by examining "sample diversity". This concept is commonly examined in the deep generative modeling field, and when applied to computer vision problems, metrics such as Inception Score (Salimans et al. 2016) are commonly used. Here, we assess sample diversity by simply examining standard deviation, which is a valuable measure for physics-based problems. In Sec. 3a, we assessed LDM sample diversity by taking a single observation, e.g., the one in Fig 5a, and calculating the standard deviation of *u* across 100 conditionally generated samples (Fig 5e). This conditional standard deviation was calculated using samples from the LDM for a given observation. Alternatively, by applying tools such as fully connected neural networks or stochastic estimation (Hassanaly et al. 2022) to our training dataset, it is possible to estimate what the conditional standard deviation should be for a given observation, without the need to generate any samples. This function has no awareness of the LDM or the samples it generates, and as such, it serves as an external check on the sample-calculated conditional standard deviation.

Following Hassanaly et al. (2022), we obtain an external estimate (Fig 5f) of the conditional standard deviation for the observation in Fig 5a by training a fully connected neural network. We provide more details on the external estimate methodology in Appendix C. This external estimate agrees well with the LDM sample standard deviation (Fig 5e), but it fills in weaknesses that arise from calculating the sample standard deviation with a finite number of samples. The two standard deviations agree well in magnitude everywhere: the lowest grid cells, the observation network, and above the capping inversion. Both estimates also show larger variance just upwind of the meteorological mast and above the scanning lidar, a behavior that arises due to the presence of a

coherent structure. Crucially, the external estimate clearly shows that the sensing network has an impact on the flow reconstructions close to the observations, up to a maximum reach of roughly 150 m in any direction. By comparing the two standard deviations, we build confidence that the LDM doesn't show major deficiencies in terms of sample diversity. This result complements the rank histogram analysis, suggesting that indeed the LDM is only slightly underly diverse.

5. Conclusion

In this study, we lay the groundwork for microscale data assimilation in the context of the RAAW field campaign. We are interested in eventually carrying out ensemble-based data assimilation, but we face a challenge—given field campaign measurements, there is no standard approach to initialize large-eddy simulation codes for ensemble-based data assimilation. Here, we address this problem with use of a latent diffusion model (LDM), a recently developed deep generative modeling algorithm, to generate initial conditions that match observations.

We assess the performance of our LDMs using qualitative visualizations, physics-based characteristics, and ensemble-forecasting metrics. We find that our LDMs produce sufficiently accurate turbulent structures on large and moderate spatial scales, while inaccurately modeling the smallest scales. Even given this limitation, our large-eddy simulation code successfully runs without any obvious artifacts when using LDM samples as initial conditions. The LDM successfully generates a diverse ensemble of samples when given a synthetic observation. Ensembles show near-zero bias relative to ground truth in an unobserved location in the vicinity of observations. When conducting ensemble-oriented analysis, we find that ensembles show slightly too little member-to-member spread relative to an ideal ensemble. These deficiencies may be small in practice, and future work will couple the LDM initial conditions with a data assimilation algorithm to judge their performance. All in all, we are optimistic about the LDMs' performance for our flow reconstruction problem.

This study suggests several lines of possible future inquiry within the geosciences. As previously discussed, we plan to perform microscale ensemble-based data assimilation, first conducting simulation-based studies and then field campaign-based studies. Our code could also directly be applied to study mesoscale and synoptic-scale data assimilation. While we specifically view flow reconstruction as an inpainting problem and condition the LDM by concatenating synthetic

gridded observations, LDMs contain a more flexible conditioning mechanism that could integrate diverse information. Diffusion model researchers are investigating methods for quicker sampling (e.g., Meng et al. 2022), which could potentially open the road to real-time flow reconstruction. While we were limited to moderate sized samples (128, 128, 64) due to hardware limitations, we believe that LDMs will successfully scale to much larger samples in the near future. In the end, we believe that diffusion models are a powerful class of machine learning algorithm that is worthy of further exploration within the Earth sciences.

Acknowledgments. This work was authored in part by the National Renewable Energy Laboratory, operated by Alliance for Sustainable Energy, LLC, for the U.S. Department of Energy (DOE) under Contract No. DE-AC36-08GO28308. Funding provided by the U.S. Department of Energy Office of Energy Efficiency and Renewable Energy Wind Energy Technologies Office. The views expressed in the article do not necessarily represent the views of the DOE or the U.S. Government. The U.S. Government retains and the publisher, by accepting the article for publication, acknowledges that the U.S. Government retains a nonexclusive, paid-up, irrevocable, worldwide license to publish or reproduce the published form of this work, or allow others to do so, for U.S. Government purposes.

The research was performed using computational resources sponsored by the Department of Energy's Office of Energy Efficiency and Renewable Energy and located at the National Renewable Energy Laboratory. This work would not have been possible without several open-source diffusion modeling resources, including those by HuggingFace (https://huggingface.co/blog/annotated-diffusion), Janspiry (https://github.com/Janspiry/Palette-Image-to-Image-Diffusion-Models), Walter H. L. Pinaya (https://huggingface.co/spaces/Warvito/diffusion_brain), and CompVis (https://github.com/CompVis/latent-diffusion). The analysis was performed using a number of open-source Python libraries, including numpy (Harris et al. 2020)), Xarray (Hoyer and Hamman 2017), and matplotlib (Hunter 2007). Thank you to Hristo Chipilski for helpful discussions regarding data assimilation, and Michael Kuhn for AMR-Wind support. Additionally, thank you to the editor and the reviewers in helping craft this manuscript.

Data availability statement. The configurations of the AMR-Wind simulations, our modified LDM and configurations, and the analysis scripts used in this paper will be uploaded to https://github.com/rybchuk/latent-diffusion-3d-atmopheric-boundary-layer. The training and testing data is too large to be stored on GitHub. It is stored on NREL's supercomputer or can be regenerated using AMR-Wind (https://github.com/Exawind/amr-wind).

APPENDIX A

Additional visualizations of test data and unconditional samples

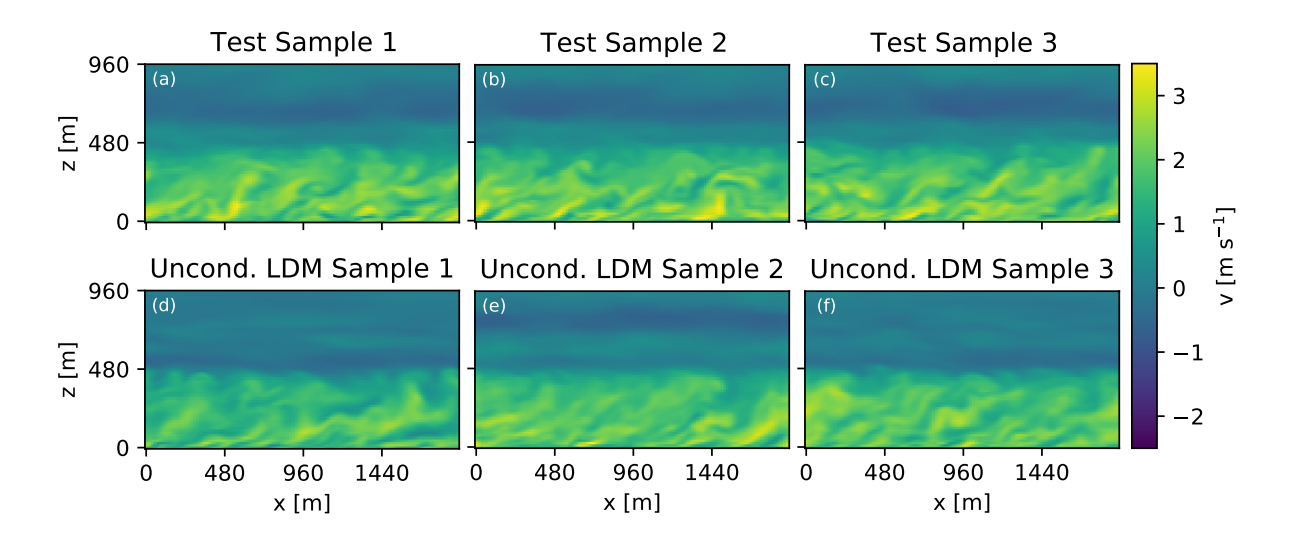


Fig. A1. Same as Figure 3, but for v.

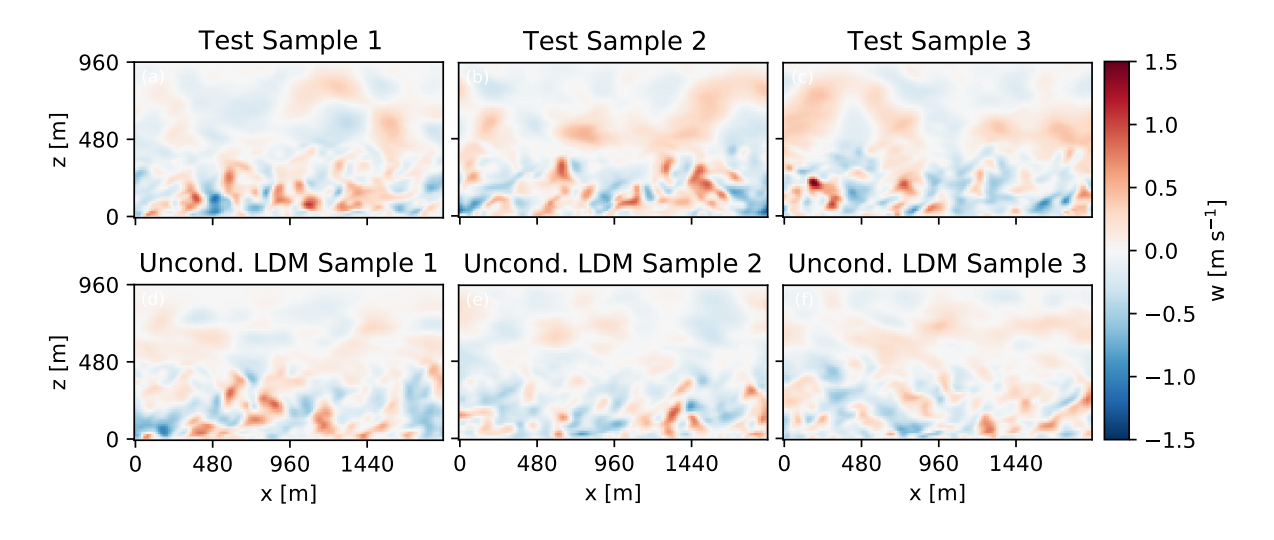


Fig. A2. Same as Figure 3, but for w.

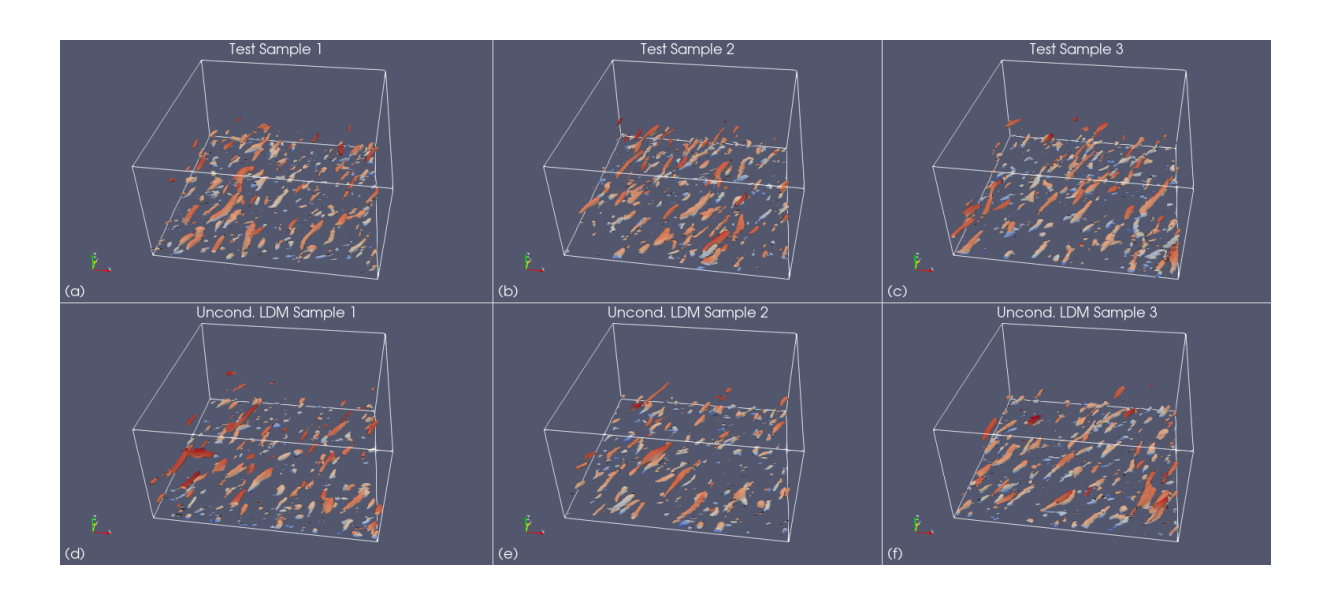


Fig. A3. Isometric views of vortices identified as contours of the Q-criterion (Jeong and Hussain 1995) with a value of $0.0003~\text{m s}^{-1}$.

APPENDIX B

Additional visualizations of box and FC conditional samples

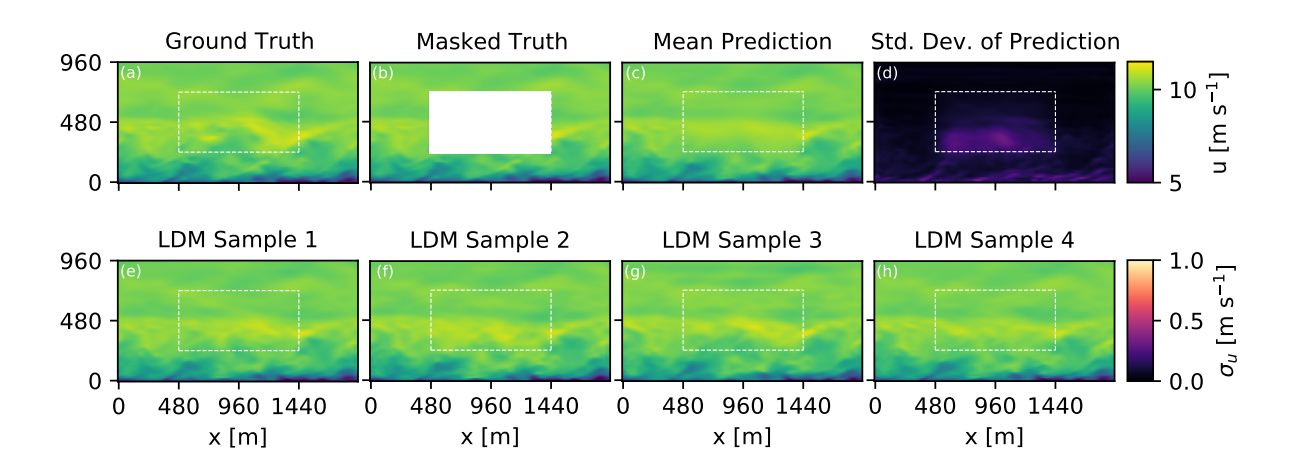


Fig. B1. A distinct (a) ground truth and (b) box observation from the one shown in Fig. 4. The (c) mean prediction and (d) standard deviation of prediction from 100 LDM samples are shown. (e)–(h) Four distinct LDM samples given the observation.

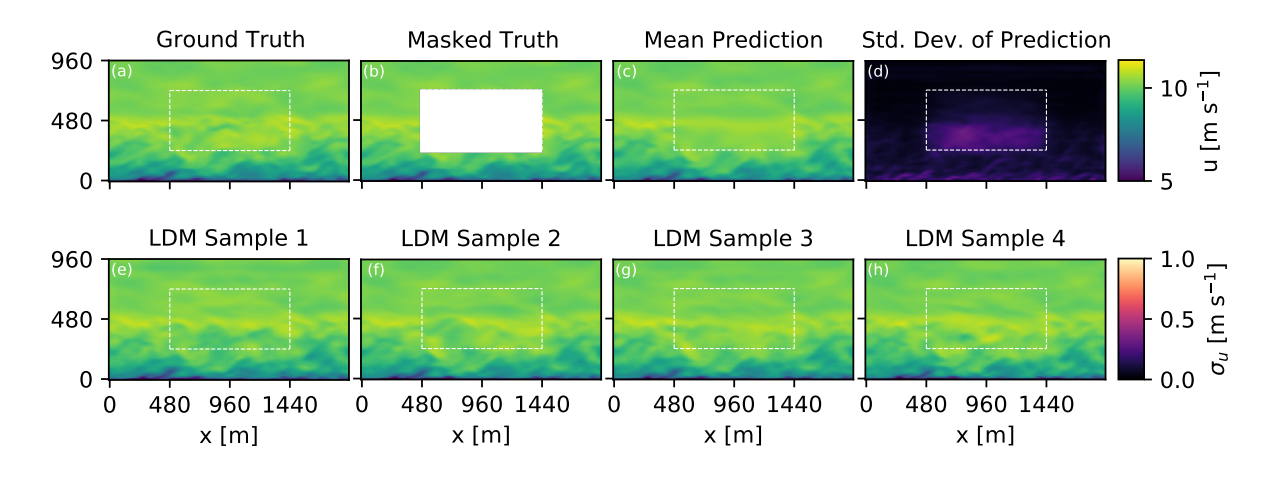


Fig. B2. Same as Fig. B1, except for a distinct observation.

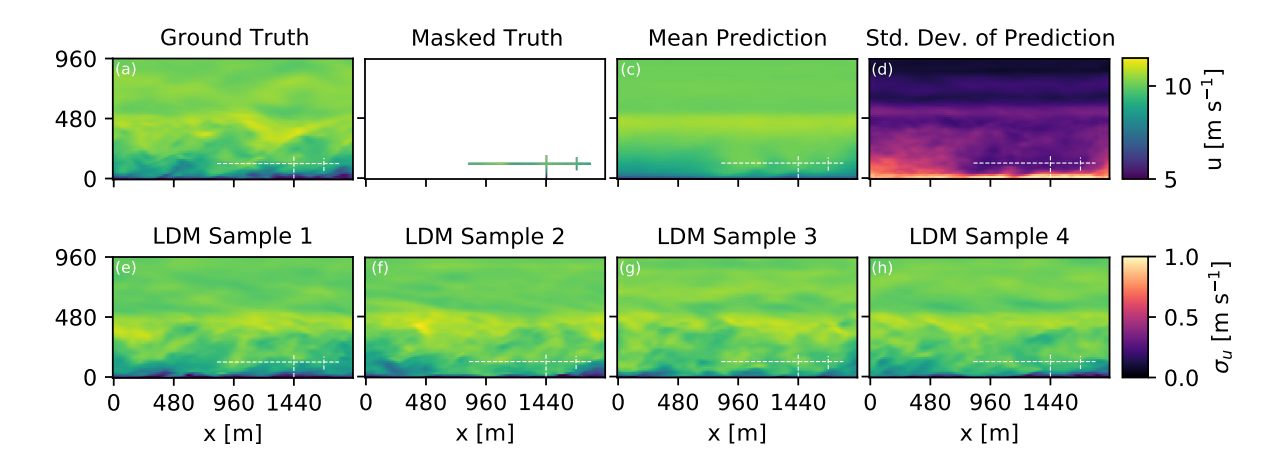


Fig. B3. Same as Fig. B1, except for the FC mask.

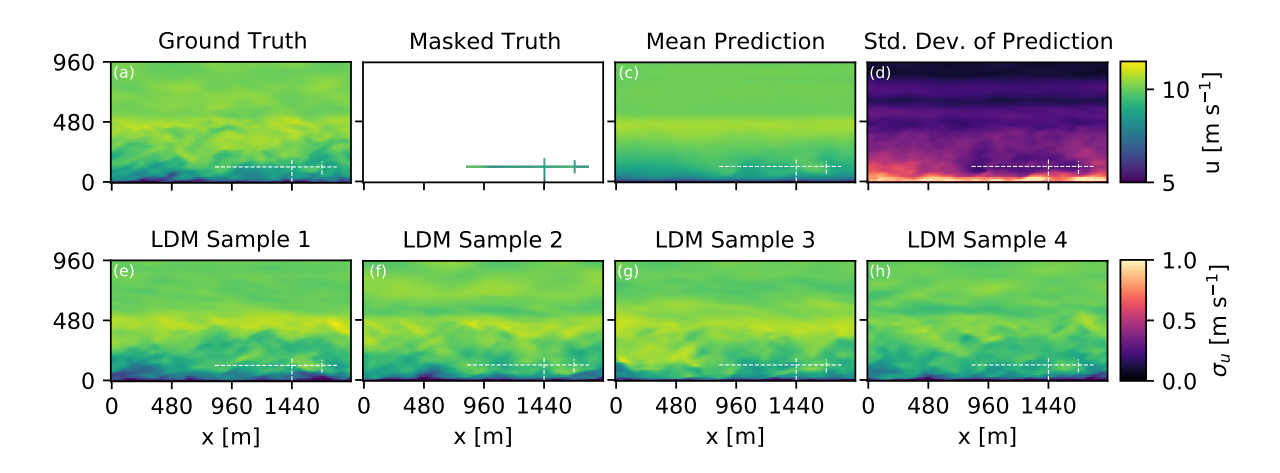


Fig. B4. Same as Fig. B3, except for a distinct observation.

APPENDIX C

Technical details for external estimates of the conditional standard deviation

The a priori moment estimation method is detailed here. Consider an observation $y \in \mathbb{R}^d$ where d is the length of the observation vector, and $x \in \mathbb{R}^m$ where m is the length of the state vector. The function f that best approximates x given y, i.e., that minimizes $||f(y) - x||_2$, is called the optimal estimator of x given y. In addition, the optimal estimator is the conditional expectation of x given y (Papoulis and Unnikrishna Pillai 2002). Therefore, by seeking the optimal estimator of x given y, one can approximate the conditional moments of x given y. Likewise, by seeking the conditional moments of x^2 given y, one can approximate the diagonal of the covariance matrix of the distribution sampled (i.e., the pointwise variance).

We obtain a priori estimates of conditional standard deviation by using a neural network. We construct the neural network to approximate the optimal estimator of the atmospheric state (for the first moment) and the square of the atmospheric state (for the second moment), given the observed field as the input. We use the architecture of Ledig et al. (2017), a fully convolutional network with residual blocks and skip connections.

To ensure that a reasonable approximation of the optimal estimator has been reached, we train multiple neural nets with increasing complexity, until the mean-square-error (MSE) loss stops improving. Similar to Hassanaly et al. (2022), we adjust two model architecture hyperparameters to converge to the optimal estimator: the number of filters per convolutional layers varied in the set $\{1,2,4,8\}$ and the number of residual blocks varied in the set $\{2,4,8,16\}$. Unlike in Hassanaly et al. (2022), the input and output of the network have the same dimension. The input is altered by setting the masked pixels to a zero value. The loss function is calculated by computing the MSE with the masked pixels only, thereby enforcing that unmasked pixels do not contribute to evaluating the conditional estimator. Since 3D convolutions are used and to accommodate memory requirements, the batch size is typically set to 8 but changed to 4 for the biggest network. A fixed learning rate of 1e-3 was used. Similar to Hassanaly et al. (2022), the second moment is estimated by outputting the square of the state substracted with the first moment. All networks considered here were sufficiently trained to reach convergence (Figure C1).

Once fully trained, the final training loss is examined to decide if further increase of network complexity is warranted to appropriately approximate the optimal estimator (Figure C2). We

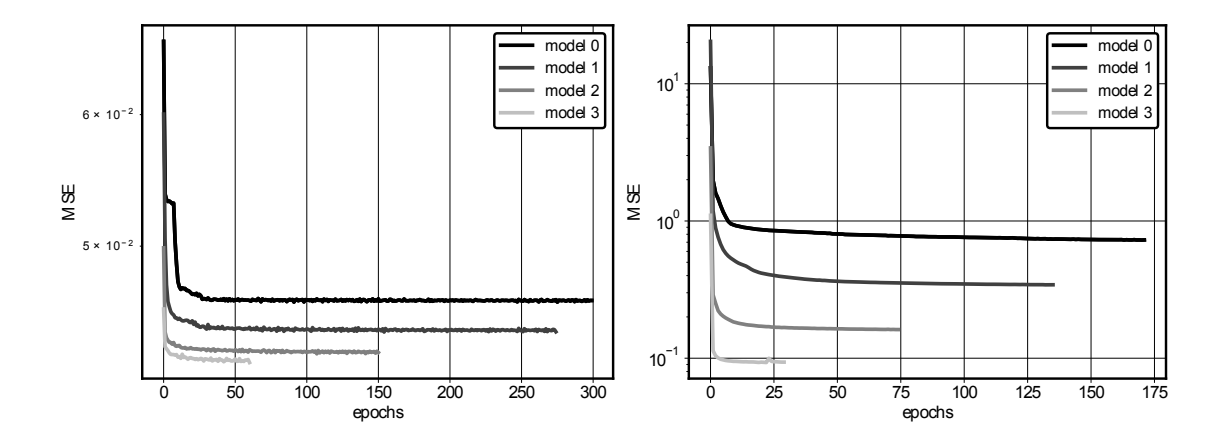


Fig. C1. MSE training loss versus epoch number for all the model architectures for FC mask for the first moment estimate (left) and the second moment estimate (right).

find that as the number of trainable parameters increases beyond approximately 9,000 to approximately 60,000, the MSE decreases until a point where adding additional trainable parameters only marginally improves the loss. As such we stop increasing the complexity of the estimator network and produce the figure shown in Fig. 5f using the model with the highest number of parameters.

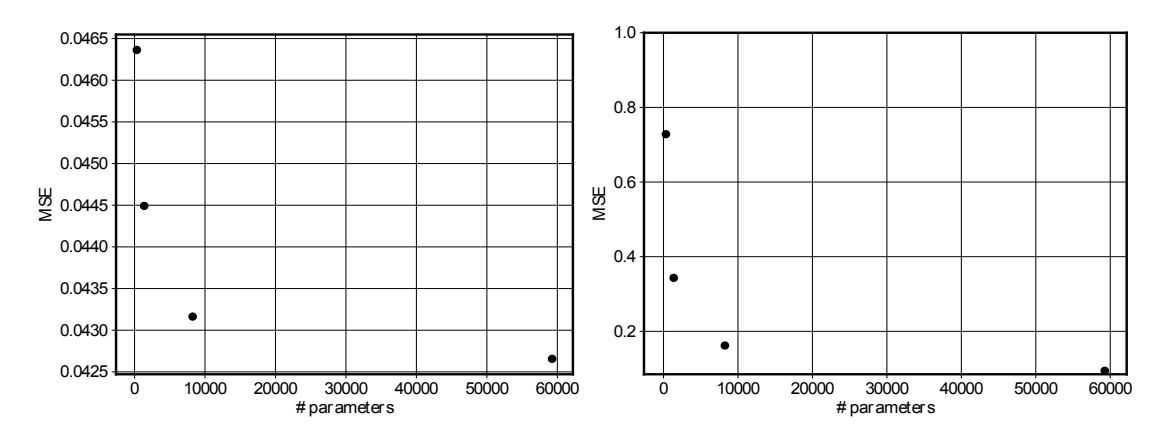


Fig. C2. Final MSE training loss versus number of trainable parameters for the FC mask for the first moment estimate (left) and the second moment estimate (right).

References

- Allaerts, D., E. Quon, C. Draxl, and M. Churchfield, 2020: Development of a Time–Height Profile Assimilation Technique for Large-Eddy Simulation. *Boundary-Layer Meteorology*, **176** (3), 329–348, https://doi.org/10.1007/s10546-020-00538-5.
- Bannister, R. N., 2017: A review of operational methods of variational and ensemble-variational data assimilation. *Quarterly Journal of the Royal Meteorological Society*, **143** (**703**), 607–633, https://doi.org/10.1002/qj.2982.
- Bauweraerts, P., and J. Meyers, 2021: Reconstruction of turbulent flow fields from lidar measurements using large-eddy simulation. *Journal of Fluid Mechanics*, **906**, A17, https://doi.org/10.1017/jfm.2020.805.
- Boorsma, K., and Coauthors, 2023: Progress in the validation of rotor aerodynamic codes using field data. *Wind Energy Science*, **8** (2), 211–230, https://doi.org/10.5194/wes-8-211-2023.
- Brock, A., J. Donahue, and K. Simonyan, 2019: arXiv:1809.11096. Large Scale GAN Training for High Fidelity Natural Image Synthesis. arXiv, https://doi.org/10.48550/arXiv.1809.11096, 1809.11096.
- Carrassi, A., M. Bocquet, L. Bertino, and G. Evensen, 2018: Data assimilation in the geosciences: An overview of methods, issues, and perspectives. *WIREs Climate Change*, **9** (**5**), e535, https://doi.org/10.1002/wcc.535.
- Defforge, C. L., B. Carissimo, M. Bocquet, R. Bresson, and P. Armand, 2019: Improving CFD atmospheric simulations at local scale for wind resource assessment using the iterative ensemble Kalman smoother. *Journal of Wind Engineering and Industrial Aerodynamics*, **189**, 243–257, https://doi.org/10.1016/j.jweia.2019.03.030.
- Dhariwal, P., and A. Nichol, 2021: Diffusion Models Beat GANs on Image Synthesis. *Advances in Neural Information Processing Systems*, Curran Associates, Inc., Vol. 34, 8780–8794.
- Di Leoni, P. C., K. Agarwal, T. Zaki, C. Meneveau, and J. Katz, 2022: arXiv:2210.04849. Reconstructing velocity and pressure from sparse noisy particle tracks using Physics-Informed Neural Networks. arXiv, https://doi.org/10.48550/arXiv.2210.04849, 2210.04849.

- Diop, M., P. Dubois, H. Toubin, L. Planckaert, J.-F. L. Roy, and E. Garnier, 2022: Reconstruction of flow around a high-rise building from wake measurements using Machine Learning techniques. *Journal of Wind Engineering and Industrial Aerodynamics*, **230**, 105 149, https://doi.org/10.1016/j.jweia.2022.105149.
- Doubrawa, P., and Coauthors, 2020: Multimodel validation of single wakes in neutral and stratified atmospheric conditions. *Wind Energy*, **23** (**11**), 2027–2055, https://doi.org/10.1002/we.2543.
- Du, Y., M. Wang, and T. A. Zaki, 2022: arXiv:2210.09424. State estimation in minimal turbulent channel flow: A comparative study of 4DVar and PINN. arXiv, 2210.09424.
- Evensen, G., and Coauthors, 2009: *Data Assimilation: The Ensemble Kalman Filter*, Vol. 2. Springer.
- Fukami, K., K. Fukagata, and K. Taira, 2019: Super-resolution reconstruction of turbulent flows with machine learning. *Journal of Fluid Mechanics*, **870**, 106–120, https://doi.org/10.1017/jfm. 2019.238.
- Goodfellow, I. J., J. Pouget-Abadie, M. Mirza, B. Xu, D. Warde-Farley, S. Ozair, A. Courville, and Y. Bengio, 2014: arXiv:1406.2661. Generative Adversarial Networks. arXiv, https://doi.org/10.48550/arXiv.1406.2661, 1406.2661.
- Hamill, T. M., 2001: Interpretation of Rank Histograms for Verifying Ensemble Forecasts. *Monthly Weather Review*, **129** (3), 550–560, https://doi.org/10.1175/1520-0493(2001) 129<0550:IORHFV>2.0.CO;2.
- Hamilton, N., P. Doubrawa, J. Naughton, and C. Kelley, 2022: Rotor aerodynamics, aeroelastics, and wake (RAAW) campaign overview. *Bulletin of the American Physical Society*.
- Harris, C. R., and Coauthors, 2020: Array programming with NumPy. *Nature*, **585** (**7825**), 357–362, https://doi.org/10.1038/s41586-020-2649-2.
- Hassanaly, M., A. Glaws, K. Stengel, and R. N. King, 2022: Adversarial sampling of unknown and high-dimensional conditional distributions. *Journal of Computational Physics*, **450**, 110 853, https://doi.org/10.1016/j.jcp.2021.110853.

- He, K., X. Zhang, S. Ren, and J. Sun, 2016: Deep residual learning for image recognition. *Proceedings of the IEEE Conference on Computer Vision and Pattern Recognition*, 770–778.
- Hoyer, S., and J. Hamman, 2017: Xarray: N-D labeled Arrays and Datasets in Python. *Journal of Open Research Software*, **5** (1), 10, https://doi.org/10.5334/jors.148.
- Hunter, J. D., 2007: Matplotlib: A 2D Graphics Environment. *Computing in Science Engineering*, **9** (3), 90–95, https://doi.org/10.1109/MCSE.2007.55.
- Isola, P., J.-Y. Zhu, T. Zhou, and A. A. Efros, 2018: arXiv:1611.07004. Image-to-Image Translation with Conditional Adversarial Networks. arXiv, https://doi.org/10.48550/arXiv.1611.07004, 1611.07004.
- Jeong, J., and F. Hussain, 1995: On the identification of a vortex. *Journal of Fluid Mechanics*, **285**, 69–94, https://doi.org/10.1017/S0022112095000462.
- Kawar, B., M. Elad, S. Ermon, and J. Song, 2022: Denoising Diffusion Restoration Models. https://doi.org/10.48550/arXiv.2201.11793.
- Kingma, D. P., and M. Welling, 2013: Auto-Encoding Variational Bayes. https://doi.org/10.48550/arXiv.1312.6114.
- Labahn, J. W., H. Wu, S. R. Harris, B. Coriton, J. H. Frank, and M. Ihme, 2020: Ensemble Kalman Filter for Assimilating Experimental Data into Large-Eddy Simulations of Turbulent Flows. *Flow, Turbulence and Combustion*, **104** (**4**), 861–893, https://doi.org/10.1007/s10494-019-00093-1.
- Ledig, C., and Coauthors, 2017: Photo-realistic single image super-resolution using a generative adversarial network. *Proceedings of the IEEE Conference on Computer Vision and Pattern Recognition (CVPR)*.
- Lorenz, E. N., 1963: Deterministic Nonperiodic Flow. *Journal of the Atmospheric Sciences*, **20** (2), 130–141, https://doi.org/10.1175/1520-0469(1963)020<0130:DNF>2.0.CO;2.
- Lugmayr, A., M. Danelljan, A. Romero, F. Yu, R. Timofte, and L. Van Gool, 2022: RePaint: Inpainting Using Denoising Diffusion Probabilistic Models. *Proceedings of the IEEE/CVF Conference on Computer Vision and Pattern Recognition*, 11 461–11 471.

- Luo, C., 2022: arXiv:2208.11970. Understanding Diffusion Models: A Unified Perspective. arXiv, https://doi.org/10.48550/arXiv.2208.11970, 2208.11970.
- Meng, C., R. Rombach, R. Gao, D. P. Kingma, S. Ermon, J. Ho, and T. Salimans, 2022: arXiv:2210.03142. On Distillation of Guided Diffusion Models. arXiv, https://doi.org/10.48550/arXiv.2210.03142, 2210.03142.
- Monache, L. D., F. A. Eckel, D. L. Rife, B. Nagarajan, and K. Searight, 2013: Probabilistic Weather Prediction with an Analog Ensemble. *Monthly Weather Review*, **141** (**10**), 3498–3516, https://doi.org/10.1175/MWR-D-12-00281.1.
- Mons, V., J. C. Chassaing, T. Gomez, and P. Sagaut, 2016: Reconstruction of unsteady viscous flows using data assimilation schemes. *Journal of Computational Physics*, **316**, 255–280, https://doi.org/10.1016/j.jcp.2016.04.022.
- National Research Council, 2012: Assessing the Reliability of Complex Models: Mathematical and Statistical Foundations of Verification, Validation, and Uncertainty Quantification. National Academies Press.
- Papoulis, A., and S. Unnikrishna Pillai, 2002: *Probability, Random Variables and Stochastic Processes*.
- Pinaya, W. H. L., P.-D. Tudosiu, J. Dafflon, P. F. da Costa, V. Fernandez, P. Nachev, S. Ourselin, and M. J. Cardoso, 2022: arXiv:2209.07162. Brain Imaging Generation with Latent Diffusion Models. arXiv, https://doi.org/10.48550/arXiv.2209.07162, 2209.07162.
- Ravuri, S., and Coauthors, 2021: Skilful precipitation nowcasting using deep generative models of radar. *Nature*, **597** (**7878**), 672–677, https://doi.org/10.1038/s41586-021-03854-z.
- Rombach, R., A. Blattmann, D. Lorenz, P. Esser, and B. Ommer, 2022: arXiv:2112.10752. High-Resolution Image Synthesis with Latent Diffusion Models. arXiv, https://doi.org/10.48550/arXiv.2112.10752, 2112.10752.
- Ronneberger, O., P. Fischer, and T. Brox, 2015: arXiv:1505.04597. U-Net: Convolutional Networks for Biomedical Image Segmentation. arXiv, https://doi.org/10.48550/arXiv.1505.04597, 1505. 04597.

- Saharia, C., W. Chan, H. Chang, C. A. Lee, J. Ho, T. Salimans, D. J. Fleet, and M. Norouzi, 2022: arXiv:2111.05826. Palette: Image-to-Image Diffusion Models. arXiv, 2111.05826.
- Salimans, T., I. Goodfellow, W. Zaremba, V. Cheung, A. Radford, X. Chen, and X. Chen, 2016: Improved Techniques for Training GANs. Advances in Neural Information Processing Systems, Curran Associates, Inc., Vol. 29.
- Schepers, G., 2021: IEA Task 47 Innovative aerodynamic experiment technologies and simulations on wind turbines in turbulent inflow Gerard. https://doi.org/10.5281/zenodo.4580359.
- Sohl-Dickstein, J., E. Weiss, N. Maheswaranathan, and S. Ganguli, 2015: Deep Unsupervised Learning using Nonequilibrium Thermodynamics. *Proceedings of the 32nd International Conference on Machine Learning*, PMLR, 2256–2265.
- Song, Y., and S. Ermon, 2020: arXiv:1907.05600. Generative Modeling by Estimating Gradients of the Data Distribution. arXiv, https://doi.org/10.48550/arXiv.1907.05600, 1907.05600.
- Song, Y., J. Sohl-Dickstein, D. P. Kingma, A. Kumar, S. Ermon, and B. Poole, 2021: arXiv:2011.13456. Score-Based Generative Modeling through Stochastic Differential Equations. arXiv, https://doi.org/10.48550/arXiv.2011.13456, 2011.13456.
- Sprague, M. A., 2021: ExaWind: Predictive wind energy simulations. Tech. rep., National Renewable Energy Lab.(NREL), Golden, CO (United States).
- Stengel, K., A. Glaws, D. Hettinger, and R. N. King, 2020: Adversarial super-resolution of climatological wind and solar data. *Proceedings of the National Academy of Sciences*, **117** (**29**), 16 805–16 815, https://doi.org/10.1073/pnas.1918964117.
- Stoll, R., J. A. Gibbs, S. T. Salesky, W. Anderson, and M. Calaf, 2020: Large-Eddy Simulation of the Atmospheric Boundary Layer. *Boundary-Layer Meteorology*, **177** (2), 541–581, https://doi.org/10.1007/s10546-020-00556-3.
- Suvorov, R., and Coauthors, 2022: Resolution-robust large mask inpainting with fourier convolutions. *Proceedings of the IEEE/CVF Winter Conference on Applications of Computer Vision (WACV)*, 2149–2159.

- Ulyanov, D., A. Vedaldi, and V. Lempitsky, 2017: arXiv:1607.08022. Instance Normalization: The Missing Ingredient for Fast Stylization. arXiv, https://doi.org/10.48550/arXiv.1607.08022, 1607.08022.
- Vetra-Carvalho, S., P. J. van Leeuwen, L. Nerger, A. Barth, M. U. Altaf, P. Brasseur, P. Kirchgessner, and J.-M. Beckers, 2018: State-of-the-art stochastic data assimilation methods for high-dimensional non-Gaussian problems. *Tellus A: Dynamic Meteorology and Oceanography*, **70** (1), 1–43, https://doi.org/10.1080/16000870.2018.1445364.
- Wang, Q., M. Wang, and T. A. Zaki, 2022: What is observable from wall data in turbulent channel flow? *Journal of Fluid Mechanics*, **941**, https://doi.org/10.1017/jfm.2022.295.
- Wilks, D. S., 2019: Statistical Methods in the Atmospheric Sciences. *Statistical Methods in the Atmospheric Sciences (Fourth Edition)*, Elsevier, i–ii, https://doi.org/10.1016/B978-0-12-815823-4.09987-9.
- Wu, Y., and K. He, 2018: arXiv:1803.08494. Group Normalization. arXiv, https://doi.org/10.48550/arXiv.1803.08494, 1803.08494.
- Xiao, Z., K. Kreis, and A. Vahdat, 2022: arXiv:2112.07804. Tackling the Generative Learning Trilemma with Denoising Diffusion GANs. arXiv, https://doi.org/10.48550/arXiv.2112.07804, 2112.07804.
- Yousif, M. Z., L. Yu, and H.-C. Lim, 2021: High-fidelity reconstruction of turbulent flow from spatially limited data using enhanced super-resolution generative adversarial network. *Physics of Fluids*, **33** (**12**), 125 119, https://doi.org/10.1063/5.0066077.
- Yu, L., M. Z. Yousif, M. Zhang, S. Hoyas, R. Vinuesa, and H.-C. Lim, 2022: Three-dimensional ESRGAN for super-resolution reconstruction of turbulent flows with tricubic interpolation-based transfer learning. *Physics of Fluids*, **34** (**12**), 125 126, https://doi.org/10.1063/5.0129203.
- Zaki, T. A., and M. Wang, 2021: From limited observations to the state of turbulence: Fundamental difficulties of flow reconstruction. *Physical Review Fluids*, **6** (**10**), 100 501, https://doi.org/10.1103/PhysRevFluids.6.100501.

Zhang, R., P. Isola, A. A. Efros, E. Shechtman, and O. Wang, 2018: arXiv:1801.03924. The Unreasonable Effectiveness of Deep Features as a Perceptual Metric. arXiv, https://doi.org/10.48550/arXiv.1801.03924, 1801.03924.